Microchim Acta (2016) 183:1019–1032
DOI 10.1007/s00604-015-1701-7

REVIEW ARTICLE

Nanopore-enabled electrode arrays and ensembles

Lawrence P. Zaino III[1] · **Chaoxiong Ma**[1] · **Paul W. Bohn**[1,2]

Received: 31 August 2015 / Accepted: 1 December 2015 / Published online: 29 December 2015

Abstract This review (with 116 refs.) addresses recent developments in nanoelectrode arrays and ensembles with particular attention to nanopore-enabled arrays and ensembles. Nanoelectrode-based arrays exhibit unique mass transport and ion transfer properties, which can be exploited for electroanalytical measurements with enhanced figures-of-merit with respect to microscale and larger components. Following an introduction into the topic, we cover (a) methods for fabrication of solid-state nanopore electrodes, (b) chemical and biochemical sensors, (c) nanochannel arrays with embedded nanoelectrodes; (d) recessed nanodisk electrode arrays; (e) redox cycling in nanopore electrode arrays, (f) finally discuss novel nanoarrays for electrochemistry, and then give a future outlook. A wide variety of nanoelectrode array-based chemical and biochemical sensors properties are discussed in addition to faradaic, ion transfer and spectroelectrochemical applications.

Keywords Nanoelectrode · Nanopore · Recessed nanodisk · Nanochannel array · Redox cycling · Biosensor

Introduction

From nanopore battery arrays to diamond nanoelectrode arrays, advances in nanoelectrochemistry have been both rapid and extensive due to the beneficial properties gained from reducing electrode size to the nanoscale. [1–4] Recent reviews have covered the current state of nanoelectrochemistry. [3, 5–7] Nanoelectrodes are of particular interest due to properties such as decreased charging currents and increased spatial resolution. In recent years, research in nanoelectrochemistry has begun to address highly multiplexed measurements [8], electrochemistry in nanoscopic volumes [9] and nanoporous electrodes. [10] These interests intersect with the development of nanoelectrode arrays, particularly nanopore-electrode based arrays and ensembles. Interest in nanoelectrode arrays began with the work of Martin and coworkers, who developed nanoelectrode ensembles based on the nanoporous structure of track-etched membranes. Collections (arrays, ensembles) of nanoelectrodes such as these are of interest for many reasons; they exhibit macroscopic electrode area, and they support large currents, while retaining the unique mass transport features that accrue to nanoscale electrodes.

In this review, consistent with general use in the literature, *array* will be used to describe spatially ordered collections of nanoelectrodes, whereas *ensemble* will be used to describe random or stochastic collections of nanoelectrodes. Arrays and ensembles of electrodes are of particular interest due to the way that their properties depend on geometry, size, spacing, etc. [11–19] In particular, mass transport can be drastically affected by these properties. For example, the behavior of nanoelectrode arrays varies with electrode size, interelectrode distance, timescale, and diffusion zone overlap, the latter determining whether the array behaves as one large electrode or each nanoelectrode experiences enhanced radial diffusion. The size and geometry of the electrode also present interesting opportunities to control mass transport by manipulating electrostatic screening and coupling to electrokinetic flow.

A subset of nanoelectrodes are those that are integrated with solid-state nanopores, a class of structures which has

✉ Paul W. Bohn
pbohn@nd.edu

[1] Department of Chemistry and Biochemistry, University of Notre Dame, Notre Dame, IN 46556, USA

[2] Department of Chemical and Biomolecular Engineering, University of Notre Dame, Notre Dame, IN 46556, USA

demonstrated a versatile set of capabilities based on manipulating mass transport, ion transfer, and multiplexing with spectroscopic measurements. This particularly active area of current nanoelectrode array research, especially arrays and ensembles of nanopore electrodes, will be the primary focus of this review. In nanopore electrode arrays, electrodes are embedded in nanochannels or nanopores oriented either vertically or horizontally, depending on the intended end use. Nanopore electrode arrays exhibit interesting and useful properties, especially for applications in electroanalytical chemistry, e.g. redox cycling, and electrochemical processing, e.g. cascade reactions.

Fabrication

In current practice, solid-state nanopore electrode arrays are fabricated using either serial, e.g. direct-write electron beam lithography (EBL), ion beam milling, [20–24] or parallel, e.g. lithography/etching-based methods, [25–27] in contrast to early nanoelectrode arrays that were typically developed from adventitious substrates, such as porous alumina membranes. [28–31] While powerful, these fabrication methods are expensive and demand exacting conditions. To circumvent these challenges, a great deal of recent research has targeted the development of cheap, fault-tolerant routes to nanopore electrode fabrication. A common method involves colloidal (nanosphere) lithography, as depicted in Fig. 1. [32] In this approach, organized self-assembled layers of microparticles (typically polystyrene) are used as a mask to pattern the electrode array. While simple and robust, more complex structures typically demand advanced fabrication approaches. Figure 2 shows an example of multiple electrode layers fabricated into nanopore electrode arrays with pore sizes <20 nm in diameter, [33] using integrated circuit fabrication techniques. While the challenges and approaches to fabrication could justify its own review, the remainder of the review will focus on applications of nanoelectrode arrays - particularly redox cycling, coupled spectroscopy-electrochemistry, and biosensing.

Chemical and biochemical sensors

The properties of nanoelectrode arrays have naturally been exploited in developing new types of sensors with lower limits of detection (LOD). Sensors to address biomolecules have been targeted to glutamate [34], glucose [35–38], H_2O_2 [39–43], DNA, prostate specific antigen [44], dopamine [45] and lipids [46] as well as to study enzyme reactivity [36, 47]. Carbon nanofiber arrays are among the most popular electrode structures for these types of measurements due to the ease with which the surface chemistry can be tuned. [34, 45, 48, 49] For example, sensors capable of DNA detection have been fabricated as nanoelectrode arrays with DNA-selective surface functionalization. In these structures, the interaction of DNA with surface molecules limits diffusion or ion migration resulting in a decrease in electrochemical current. [50] Alternatively, monitoring ion flux though arrays of nanochannels has permitted DNA detection down to 0.1 nM. [51] Progressively lower detection limits of small metabolites, e.g. H_2O_2, down to 10^{-9} M, have also been achieved with nanoelectrode arrays, which exhibit a linear response over a large concentration range as well. [39–43] In addition to using faradaic electrochemistry, other properties of nanoelectrode arrays can be exploited for biomolecular analysis. For example, Fig. 3 shows the change in resistance of a carbon nanofiber array as a function of cardiac troponin-I concentration. Label free carbon fiber nanoelectrode arrays have demonstrated LODs (0.2 ng/mL) lower than conventional ELISA. [52]

On the non-biological side, environmental monitoring of water pollutants has been achieved with membrane-based electrochemical nanoarray sensors. Differential pulse anodic stripping is able to resolve both Pb and Cu while maintaining excellent limits of detection (0.4 μM). Furthermore, these sensors are able to quantify Cu and formaldehyde, common water source pollutants, directly in environmental samples without further clean up. [53] Similarly, carbon nanotube electrode arrays have been exploited to detect heavy metals such Cd and Pb at levels <1 ppb. [54].

Nanochannel arrays with embedded nanoelectrodes

Embedded nanoelectrodes in nanochannels are nanopore devices that are particularly interesting for lab-on-a-chip applications. Arrays on elongated nanopore (or nanochannel) arrays with embedded annular nanoband electrodes (EANE) can be fabricated with layer-by-layer deposition, followed by FIB milling. [55] Images of a typical device are shown in Fig. 4(a-c), while Fig. 4(d-e) shows SEM cross sections of the array. This class of nanopore array exhibits unique behavior in which mass transport is coupled to electrochemical processing. Alternating layers of Au and polymer permit voltage across the separate Au layers to drive electrokinetic flow, which increases the analyte delivery to the electrode surface, while the same small voltage can affect electron transfer at the EANE working electrode. By separating the EANE and a quasireference electrode, constituted by a separate metal layer (i.e. top layer of structure in Fig. 4d), in a nanopore by approximately 10 μm, electric fields, $E \sim 10^3$ V cm^{-1} can be generated from ~1 V potentials and has been shown to enhance the steady state current by as much as 50× compared to redox processes in the absence of electroosmotic flow (EOF). These array-based devices show promise for analyte processing. Due to the extremely short diffusion lengths, approximately 100 % conversion efficiency can be obtained at

suitably large dimensionless electrode width, *W*, and Peclet number, *Pe*, defined as, [56]

$$W = \frac{w}{R} \tag{1}$$

and

$$Pe = \frac{u_{avg}R}{D} \tag{2}$$

where w is the physical electrode width, R is the pore radius, u_{avg} is the linear fluid velocity averaged over the radial dimension of the pore, and D is the diffusion coefficient of the redox-active species. When EOF is turned on in these structures, the electrochemical processing is rapid and nearly perfectly efficient, resulting in the collapse of the usual diffusion layer, since redox active species are reacted as fast as they can be delivered to the EANE. Clearly under these circumstances, the reaction velocity is limited by how fast reactants can be delivered by EOF, which, in turn, is limited by the magnitude of the driving potential. To decouple EOF from the potential driving electron transfer and achieve the same high overall reaction velocities, electrokinetic flow can be controlled with a second working electrode, located external to the nanopore, leading to current increase of ~30×. [57] Furthermore, this scheme can be used with separate functions assigned to the different electrodes. For example, the upstream electrode can be used for reagent generation, as demonstrated by the upstream in situ generation of H_2 for downstream catalysis. [58].

Recessed nanodisk electrode arrays

The nanopore arrays discussed above are examples of 1D nanostructures, since there is one dimension, length, which is not nanoscale. Another interesting class is composed of 0D nanostructures, in which all three critical dimensions are nanoscale. An example of 0D nanostructures are recessed nanodisk electrode arrays, which consist of arrays non-conductive nanopores with a recessed metal disk at the bottom of each pore functioning as the electrode. These devices are of particular interest due to their unique mass transport properties, namely they provide the ability to study and exploit confinement. [59–63] Common strategies of fabrication of these types of structures include preparing them from tracked-etch membranes, processing diblock copolymers and using nanosphere lithography (vide supra). [31, 32, 64] Recessed nanopores with diameters down to 10 nm have been produced from track-etched membranes. [65] Arrays of nanopores can access a variety of diffusional regimes at different time scales, as illustrated schematically in Fig. 5. [66] At fast scan rates, peak shaped voltammograms are expected, as linear diffusion within the pores occurs without any overlap of diffusion zones between the pores. As the scan rate is decreased, sigmoidal voltammograms are observed, characteristic of radial diffusion to the pore, and as the scan rate is further decreased, diffusion zone overlap occurs between the nanopores, creating a linear diffusion regime, which again produces peak shaped voltammograms.

At fast scan rates the peak current is given by, [67]

$$i_p = 0.446nF\left(N\pi a^2\right)C\sqrt{\frac{\mathrm{nFD}\nu}{RT}} \tag{3}$$

where N is the pore density, C is concentration, n is the number of electrons, D is the diffusion coefficient, F is Faraday's constant, v is scan rate, T is temperature, a is pore radius, and R is the gas constant. Similarly, the limiting current at slow scan rates is given by, [17, 68]

$$i_{\mathrm{lim}} = \frac{4\pi \mathrm{nFCDa}\ ^2N}{4L + \pi \mathrm{a}} \tag{4}$$

where L is the pore length. Recessed nanodisk electrode arrays have numerous applications in sensing and especially in redox cycling. Emphasizing the difference in behavior relative to macroscopic planar electrodes, the small diameter of the pores and recessed nature of the electrodes make it possible to use charge screening to control mass transport to the electrode. Figure 6 shows the effect electrolyte concentration and pH have on electrostatic charge screening in arrays of 10 nm recessed nanopore electrodes. When the total electrolyte concentration is low, the opposed double layers overlap, and electrostatic interactions can either decrease or increase faradaic current, depending on the sign of the permselective behavior. At high pH, when the pore surface is negatively charged, $\zeta < 0$, an increase in current is seen from cationic analytes and a decrease is observed with anionic analytes. The dimensions of the devices are also useful in size-exclusion applications. [61] Similar types of devices, prepared from porous anodic alumina membranes, have been used to simulate the effects of confinement on biochemical reaction kinetics, [36, 69] allowing the activity of confined enzymes to be characterized using nanoporous recessed electrodes.

Redox cycling in nanopore electrode arrays

Electrode density plays an important role in the design of electrode arrays for amperometric sensing, since it governs the mass transport behavior and determines the ratio of faradic to charging current. [66] In their pioneering work, Martin and coworkers used template synthesis to fabricate nanoelectrode ensembles, which exhibited significantly decreased charging current and enhanced sensitivity. [28] In a typical amperometric measurement, diffusion behavior depends strongly on the electrode density of the electrode array or ensemble, as

illustrated in Fig. 5. In order to take advantage of the array size to achieve maximum sensitivity, an appropriate interelectrode distance should be chosen to achieve diffusional independence for individual electrodes. [67, 70] Further increasing electrode density leads to competition for analyte between adjacent electrodes due to the overlapping of diffusion zones. As a result, the limiting current decreases for an individual electrode, which can be attributed to a shielding effect and characterized by a shielding factor. [71, 72].

On the other hand, by building a structure in which it is possible to hold two adjacent electrodes negative and positive of the equilibrium potential, E_{eq}, of an electroactive species, positive feedback and an increase in faradic current can be achieved. [73–77] In such a platform, electroactive species oxidized at one electrode can diffuse to, and be reduced at, the other electrode. The cycling of redox species between the two electrodes multiplies the electron transfer reaction, resulting in current amplification at both electrodes. This redox cycling (RC) effect, which is similar to the positive feedback mode in scanning electrochemical microscopy, [78] has been observed in interdigitated electrode arrays (IDEA), [73–77] thin-layer-cells (TLC), [79–81] and planar/ring-recessed disk electrode (P/R-RDE) arrays. [26, 82–88] Here, we focus on redox cycling at P/R-RDE arrays and present some unique properties that have not been observed in other electrode geometries.

Figure 7 gives an example of the fabrication of these electrode arrays. [26, 87] In a typical electrode geometry, two thin-film gold electrodes are separated by an insulating layer, such as a polymer, SiN_x, or SiO_2 film which determines the interelectrode distance. Reliable insulation can be achieved with polymer films, but only at μm thicknesses, [89] whereas SiN_x and SiO_2 films as thin as 100 nm can provide sufficient insulation to ensure independent electrode operation. [26, 88, 90] In order to provide solution access to the bottom electrode, different lithography methods have been employed for the mask to etch the top electrode and the insulating layer. Well-defined μm-scale pores can be generated photolithographically, [89] while e-beam and nanosphere lithography can produce pores down to ~100 nm. [26, 88, 90] Multistep reactive ion etching processes can then be performed using the lithographically defined mask to access various electrode areas. [26, 87, 88].

Current amplification in RC devices The most obvious advantage of using RC is the enhancement of faradic current (Fig. 8), which can be evaluated by an amplification factor, *AF*. [74, 87] In a dual electrode system consisting of two working electrodes (WE1 and WE2), *AF* is typically calculated by *eqn.* (5),

$$AF = \frac{i_{cyc}}{i_{off}} \tag{5}$$

where i_{cyc} and i_{off} are the faradic currents obtained at the first working electrode, WE1, in RC mode with WE2 held at a potential supporting the opposite reaction, and non-RC mode (WE2 is floating), respectively. This equation can be used to evaluate the performance of P/R-RDE arrays as well as other electrode geometries.

The *AF*, a direct result of the number of redox events per unit time, depends largely on the diffusion of the redox molecules from one electrode to the other. For example, in a TLC electrode *AF* can be estimated by, [80, 91, 92]

$$AF = \frac{\pi r}{4h} \tag{6}$$

where *r* and *h* are the radius and interelectrode distance of the TLC electrode, respectively. Thus, decreasing the interelectrode distance, *h*, for a TLC electrode of a given size, *r*, produces higher *AF*. Similarly, decreasing the thickness of the insulating layer in a P/R-RDE array can also produce higher current amplification. [26, 89, 93] The dependence of *AF* on the interelectrode distance has been demonstrated from previous studies, which reported an increase of *AF* ranging from several-fold for ~μm scale *h*, [89, 93] to ~30-fold as *h* decreases to ~100 nm. [90, 94] As indicated from eqn. 6, increasing the electrode size can also produce larger current

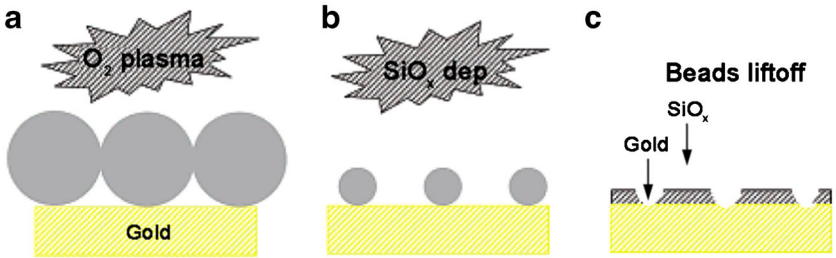

Fig. 1 Schematic illustration of the fabrication of a nanotemplate by nanosphere or colloidal lithography. **a** A monolayer of polystyrene (PS) microbeads formed at the substrate surface is subjected to an O_2 plasma etch to reduce the size of the microbeads without changing their position; **b** A masking layer is applied, here by plasma-enhanced chemical vapor deposition of SiO_x; **c** The microbeads are removed by mechanical or chemical lift-off, after which the remaining SiO_x layer may be used as a process mask for further steps. Reprinted with permission from *Anal. Chem.* 2006, 78, 7588. Copyright (2006) American Chemical Society

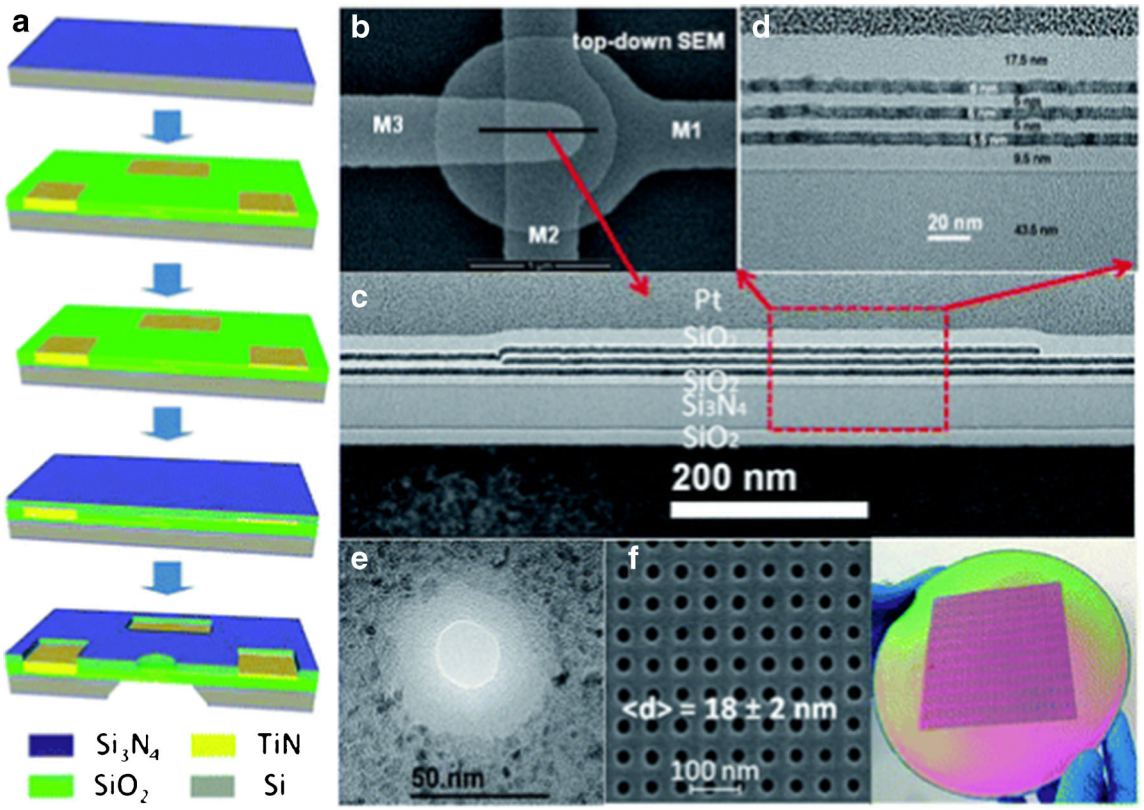

Fig. 2 **a** Schematic illustration of pore-first fabrication of 3-metal layers embedded in a nanopore membrane by reactive ion etching (RIE); *top* - substrate with nitride layers on top and bottom sides; *2nd* patterned electrodes; *3rd* - nanopore formation by RIE; *4th* - protection layers encapsulating the nanopore; *5th* - formation of the membrane by removal of the Si substrate. **b** Plan view SEM image of the region consisting of three metal layers - M3, M2, and M1, top to bottom. **c** Cross-sectional TEM image along the black line in (b) showing the uniformity of the layers over 400 nm. **d** Zoom-in of the red rectangular region in (c) shows the precise (±5 nm) control of layer thickness. **e** TEM image of a single nanopore formed by RIE. **f** SEM image showing an array of nanopores fabricated by RIE; average nanopore diameter ~ 18 ± 2 nm. **g** Integration of functional nanopores on an 8 in. wafer. Reproduced from *Nanoscale* 2014, 6, 8900. with permission of The Royal Society of Chemistry

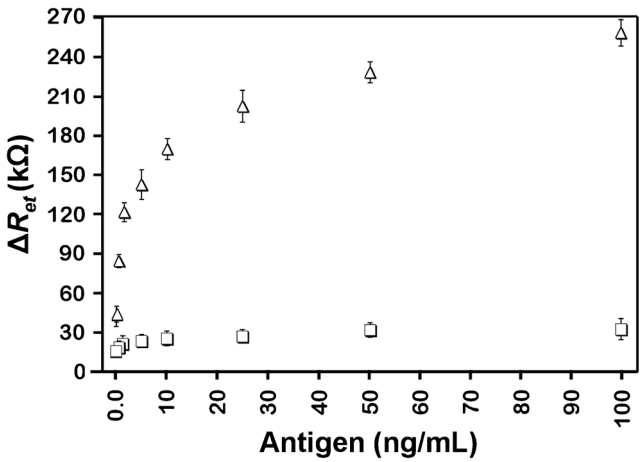

Fig. 3 Change in electron transfer resistance, ΔR_{et}, for different concentrations of human cardiac troponin-I (Δ), a specific target protein analyte, and human myoglobin (□), an unrelated nonspecific analyte for the immunosensor electrode. Reprinted with permission from *Anal. Chem.* 2013, 85, 3858. Copyright (2013) American Chemical Society

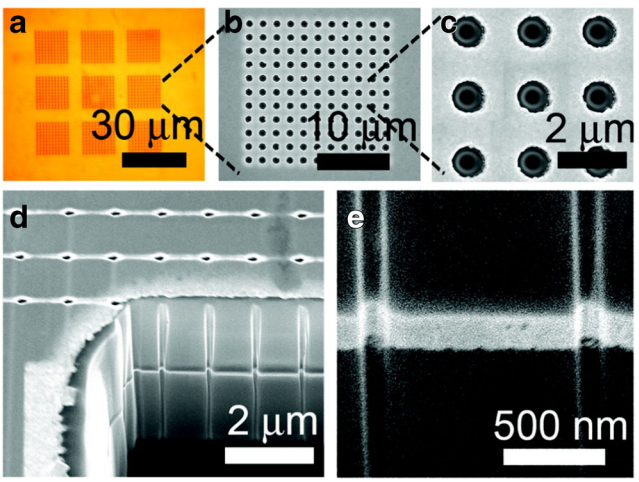

Fig. 4 Embedded annular nanoband electrode arrays. **a** Reflected light micrograph of nine pore arrays; **b** SEM image of a single 11 × 11 pore array; **c** same array at increased magnification; **d** SEM image of a sacrificial sample at 15° tilt, cross-sectioned by FIB milling; **e** magnified view of the EANE at 52° tilt. Reprinted with permission from *J. Am. Chem. Soc.* 2012, 134, 8617. Copyright (2012) American Chemical Society

amplification. This size dependence of the *AF* was demonstrated on the P/R-RDE array, where increasing electrode density results in higher collection efficiency and larger faradic current. Using smaller pores with higher density maximized the collection efficiency, resulting in current amplification up to ~50-fold. [90].

Steady-state response with small charging current Another important characteristic of the RC device is the steady-state response, Fig. 8(b), of the CVs, which is independent of the scan rate as well as the array size. [74, 89] This property is attributed to the fast mass transport occurring locally between closely-spaced electrodes. Accordingly, the number of molecules reaching the electrode surface is not limited by a diffusional boundary layer. A 2 mm × 2 mm P-RDE array has been reported to exhibit steady-state response operating in RC mode, whereas a macroscopic electrode of comparable size would exhibit diffusion limited currents. [89, 95] Furthermore, in a well-designed RC device with high collection efficiency, WE2 produces almost the same faradic current as WE1, but with much smaller charging current. For example, in an R-RDE array, charging current at the ring electrodes (WE2) held at constant potential is ~10-fold smaller than that of the disk electrode. [26] This property is especially important for high scan rate CV measurements.

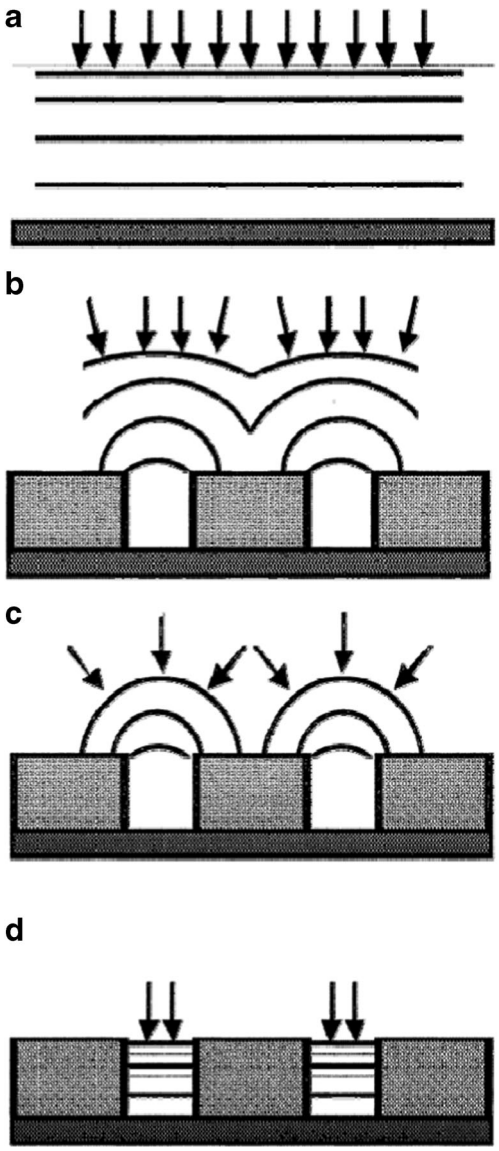

Fig. 5 Schematic illustration showing the diffusion patterns at nanopore electrodes: **a** linear diffusion to planar electrode, **b** overlapping radial diffusion to porous nanoelectrodes, **c** radial diffusion to porous nanoelectrodes, and **d** linear-active diffusion to porous nanoelectrodes. Reprinted with permission from *Langmuir* 2001, 17, 6396. Copyright (2001) American Chemical Society

Potential modulation and selectivity Since the reaction at WE1 in an RC device relies strongly on the species diffusing from WE2, it is possible to control the redox form of the species diffusing to WE1 by controlling the potential at WE2, [26, 91] as shown in Fig. 9. When the ring electrode (WE2) is held at a potential positive of E_{eq} for $Fe(CN)_6^{3/4-}$, e.g. 0.5 V vs. Ag/AgCl, oxidation of $Fe(CN)_6^{4-}$ to $Fe(CN)_6^{3-}$ occurs at WE2, whereas reduction $Fe(CN)_6^{3-}$ to $Fe(CN)_6^{4-}$ is observed on the disk electrodes (WE1). In contrast, holding WE2 at a potential negative of E_{eq}, e.g. -0.1 V, reverses redox reactions occurring at both the ring and disk electrodes. Finally, intermediate behavior with both anodic and cathodic

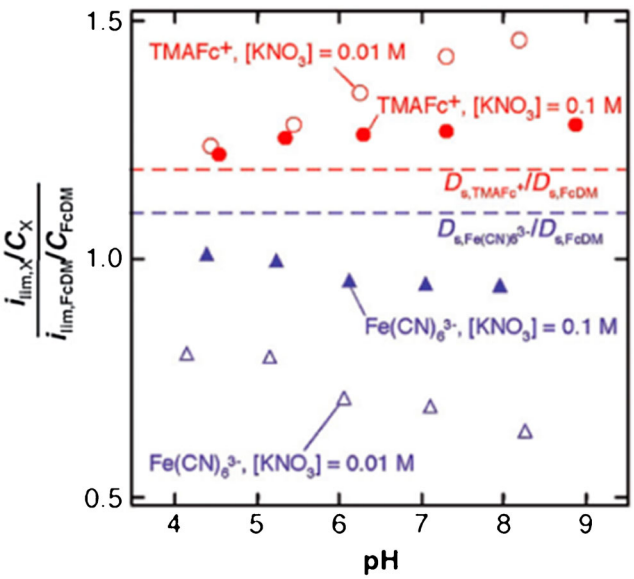

Fig. 6 pH dependence of the ratio i_{lim}/C, comparing charged redox species, X = $Fe(CN)_6^{3-}$ (triangles) or trimethylaminoferrocene ($TMAFc^+$, circles) to unchargedferrocenedimethanol, FcDM. i_{lim} values were measured at 0.01 V s^{-1} on recessed nanopore electrodes (10 nm in pore diameter) in solutions containing 0.1 M (filled symbols) or 0.01 M (open symbols) KNO_3 in addition to 0.01 M KH_2PO_4/K_2HPO_4. The ratios of the diffusion coefficients in 0.1 M KNO_3 + 0.01 M KH_2PO_4/K_2HPO_4 (pH 6.3) are shown as dashed lines. Reproduced from *Analyst* 2010, 135, 172. with permission of The Royal Society of Chemistry

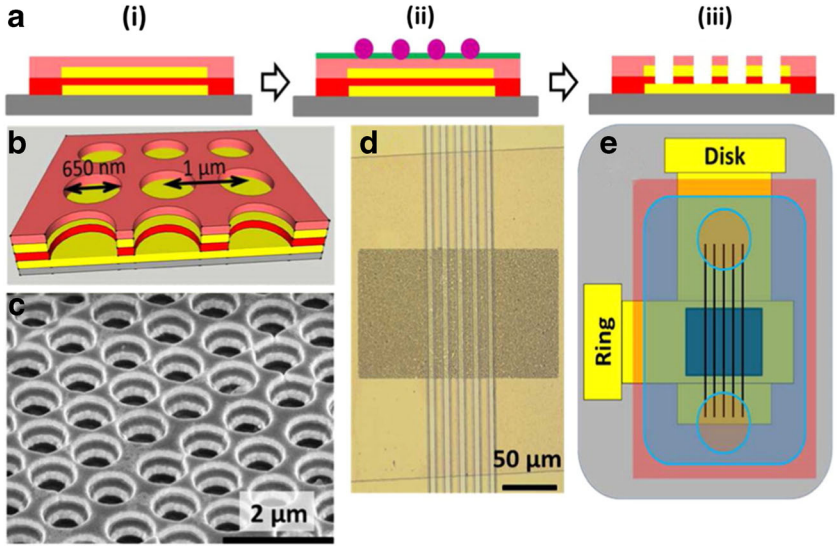

Fig. 7 **a** Schematic cross section showing the fabrication procedure for an R-RDE array, including (i) layer-by-layer deposition, (ii) nanosphere lithography, and (iii) multistep reactive ion etching. The colors represent different layers: gray (glass slide), yellow (Au), red (SiNx), pink (SiO2), purple (polystyrene spheres), and green (Cr). **b** Schematic diagram of the ring–disk geometry of the array. **c** An SEM image of the array at 50° tilt. **d** An optical image of the array integrated with SiNx channels. **e** Schematic diagram of the macroscopic layout of the R-RDE array (dark blue) integrated with channels (black) and covered by a piece of PDMS (light blue) with two circular wells. Reprinted with permission from *Anal. Chem.* 2013, 85, 9882. Copyright (2013) American Chemical Society

current collected at the rings and disk electrodes is generated if WE2 is set at an intermediate potential, e.g. +0.25 V vs. Ag/AgCl.

One application of this potential modulation is to improve measurement selectivity, which is especially important in applications that are not coupled to a separation technique. Use of the RC effect to improve selectivity depends on the reversibility of the redox reaction. Since irreversible species are not regenerated, they produce smaller faradic currents compared to reversible species under the same conditions. [80, 87, 89] In addition, an irreversible interfering species can be further depleted at the WE2 by holding it at a constant potential, enabling determination of reversible analytes at the WE1 with little interference. On the basis of this principle, selective measurement of redox reversible dopamine in the presence of irreversible ascorbic acid has been demonstrated on RC devices of different geometries. Nanoscale P/R-RDE arrays are better suited for this purpose than microscale arrays, because nanopore electrodes deplete the irreversible species more efficiently before they diffuse to and react on the disk electrode. Selectivity can be further enhanced by integrating the electrode array with micro/nanofluidic channels, which limit the amount of redox species capable of diffusing to the electrode surface, [80, 87] thereby further reducing the irreversible species in RC but not the reversible species. [26, 80, 87] Using these strategies, the measured selectivity for dopamine against ascorbic acid in an R-RDE array coupled with nanochannels was improved by 10^3x, allowing interference-free detection of dopamine in the presence of 100-fold excess of ascorbic acid. [87].

Modulation of the redox reaction can also be used to address the more challenging situation in which two reversible species with similar redox potentials must be differentiated. Although the RC effect cannot be applied directly in this situation, the potential of WE2 can be adjusted such that one species exhibits a cathodic response, while the other gives an anodic response at WE1. This principle was successfully applied to differentiate

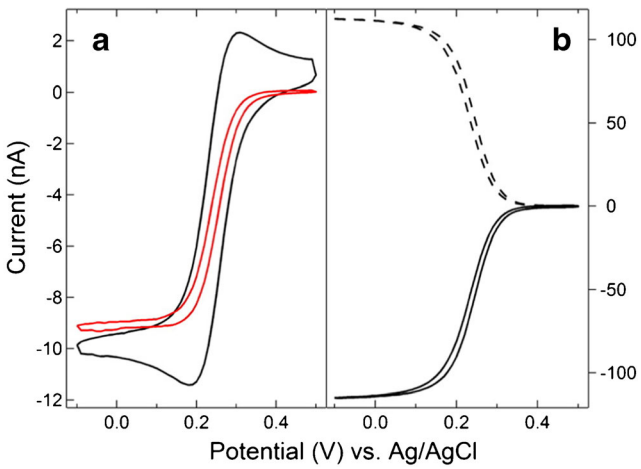

Fig. 8 Comparison of generator-collector (GC) and non-GC mode cyclic voltammograms of 1 mM $Fe(CN)_6^{3-}$ on a high density array with a 200 nm insulator separating the ring and disk electrodes. (a) Non-GC mode: ring electrodes are floating, and disk electrodes are swept at 100 mV/s (black) and 5 mV/s (red). (b) GC mode: disk (solid) and ring (dashed) current for ring electrodes held 0.5 V and disk electrodes swept at 100 mV/s. Reprinted with permission from *ACS Nano* 2013, 7, 5483. Copyright (2013) American Chemical Society

reversible species with overlapping redox potentials, such as dopamine/$Fe(CN)_6^{3-}$ and ferrocenemethanol/$Fe(CN)_6^{4-}$. [87, 96] Again, nanoscale R-RDE arrays outperform their microscale counterparts due to higher conversion ratios.

Ion accumulation and permselectivity in nanopores In RC devices, larger current amplification can be achieved by decreasing interelectrode distance or increasing electrode density. On the other hand, the pore size of P/R-RDE array has a great impact on redox cycling performance. As the diameter of the pores is reduced to a size commensurate with that of the electrical double layer, unique behaviors such as ion permselectivity and ion concentration polarization are observed. [97–100] Indeed, as a result of high surface-to-volume ratio, these effects can increase ion concentrations by several orders of magnitude. [97, 99] The ion enrichment observed in charged nanopores at low ionic strength requires very low analyte concentration and the absence of supporting electrolyte (SE) - novel conditions for electrochemical measurements. For this reason, the accumulation effect has not been employed to improve sensitivity in previous nanopore array measurements without the RC effect. Even more challenging, non-RC measurements performed in nanopores would deplete the accumulated ions before reaching steady-state current, since the number of ions, in the nanopores even at accumulated concentrations, is comparable small to those diffusing from bulk solution.

However, because the RC effect relies on redox species cycling locally between two electrodes, the localized analyte concentration, which determines the number of redox events, can benefit from ion accumulation to further improve measurement sensitivity. This concept has been demonstrated on an R-RDE array [88] using $Ru(NH_3)_6^{3+}$, which is expected to accumulate in nanopores with negative-ζ SiO_2 surfaces. Figure 10 illustrates this ion accumulation/ion permselectivity effect in increasing faradic current at low analyte concentration in the absence of SE. In contrast to the canonical electrochemical protocol which uses SE, three distinct regimes are observed in the absence of SE, revealing strong ionic strength dependence. At low analyte concentration, current enhancements as large as 100-fold arise from a combination of ion enrichment and ion migration effects. Combining these with the ~20-fold enhancement due to redox cycling yields a total current amplification ~2000-fold on the R-RDE array, making it interesting for electrochemical analysis.

Self-induced redox cycling In typical RC measurements, two electrodes are held at potentials positive and negative of E_{eq} to initiate and sustain electrochemical cycling. However, redox cycling can also occur when a powered electrode is placed adjacent to an unbiased electrode. [89, 95, 101–106] This so-called self-induced redox cycling (SIRC) relies on the bipolar behavior of the floating electrode that is coupled to the biased WE. Under these conditions, depletion of the redox

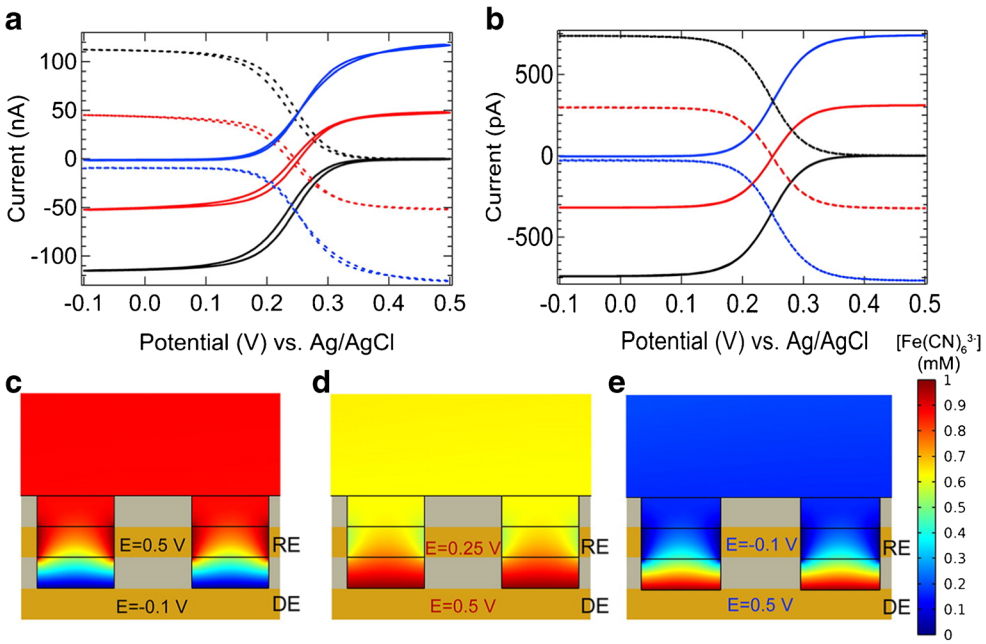

Fig. 9 **a** Ring potential dependence of the voltammetric response of 1 mM $Fe(CN)_6^{3-}$ on a high density array with 200 nm ring-disk separation. Disk electrodes are swept at 100 mV/s, and ring electrodes are held at 0.5 V (black), 0.25 V (red), and −0.1 V (blue); disk current (solid) and ring current (dashed). **b** Finite element simulated CV response of an array of 10 electrodes in 1 mM $Fe(CN)_6^{3-}$ solution on a high density array with the ring electrode held at 0.5 V (black), 0.25 V (red), and −0.1 V (blue). (**c**–**e**) Concentration profiles of $Fe(CN)_6^{3-}$ in adjacent pores with a radius of 250 nm taken from simulations of an array of 10 electrodes. The height of the insulator layers (gray) and the ring electrode (yellow) is 200 nm. Reprinted with permission from *ACS Nano* 2013, 7, 5483. Copyright (2013) American Chemical Society

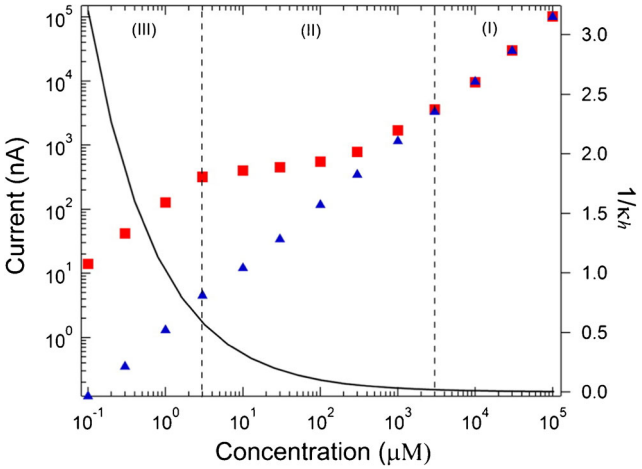

Fig. 10 Limiting ring current from voltammograms of $Ru(NH_3)_6^{3+}$ as a function of concentration both with (0.1 M KCl, blue) and without (red) supporting electrolyte. Black curve: value of 1/κh calculated at the corresponding $Ru(NH_3)_6^{3+}$ concentration in the absence of supporting electrolyte. Reprinted with permission from *J. Am. Chem. Soc.* 2014, 136, 7225. Copyright (2014) American Chemical Society

species by the biased WE produces a spatially-dependent concentration polarization relative to the adjacent floating electrode, [95, 101] which is sufficient to drive the oxidation and reduction reactions occurring respectively at opposite poles of the unbiased bipolar electrode.

Electrons flow within the bipolar electrode to balance the charge induced by the localized redox reactions, as confirmed by voltage measurements and optically observed by electrogenerated chemiluminescence. [71, 72] This electron flow can be used to couple two independent redox reactions, for example using one reaction to monitor the other. Indeed, significant sensitivity improvement was demonstrated by Yasukawa et al., who coupled the oxidation of 4-aminophenol with the reductive deposition of Ag^+, the accumulation of which was then determined by anodic stripping voltammetry. [102, 104] Recently, we explored this technique to couple RC reactions of target analytes on the P-RDE array with the electrochemical reaction of fluorigenic redox reporter systems, e.g. dihydroresorufin/resorufin. [94] The change in fluorescence intensity in the reporter system is determined by the redox reaction of the target analyte, Fig. 11. Electrochemical reduction of 1 nM $Ru(NH_3)_6^{3+}$ on the nanoelectrode array was detected by monitoring fluorescence at the remote reporter site, demonstrating the possibilities for high sensitivity electroanalytical measurements by coupling fluorigenic reporter redox reactions to self-induced redox cycling in open bipolar electrode topologies.

Novel nanoarrays for electrochemistry

Nanoscale spectroelectrochemistry Multi-modal measurements are particularly powerful since they allow information from two different sources to be correlated in a single measurement. Notably, coupling fluorescence to electrochemistry has led to a number of new measurement modalities (vide supra) with attendant improvements in sensitivity. In this regard, zeptoliter-volume metal-clad 0D nanopores are of special interest, because they can exhibit both nanoelectrochemical and nanophotonic properties simultaneously. Nanopores in an opaque metal film below a certain size cutoff exhibit zero-mode waveguide (ZMW) behavior, which produces strongly-confined, exponentially decaying evanescent fields within the

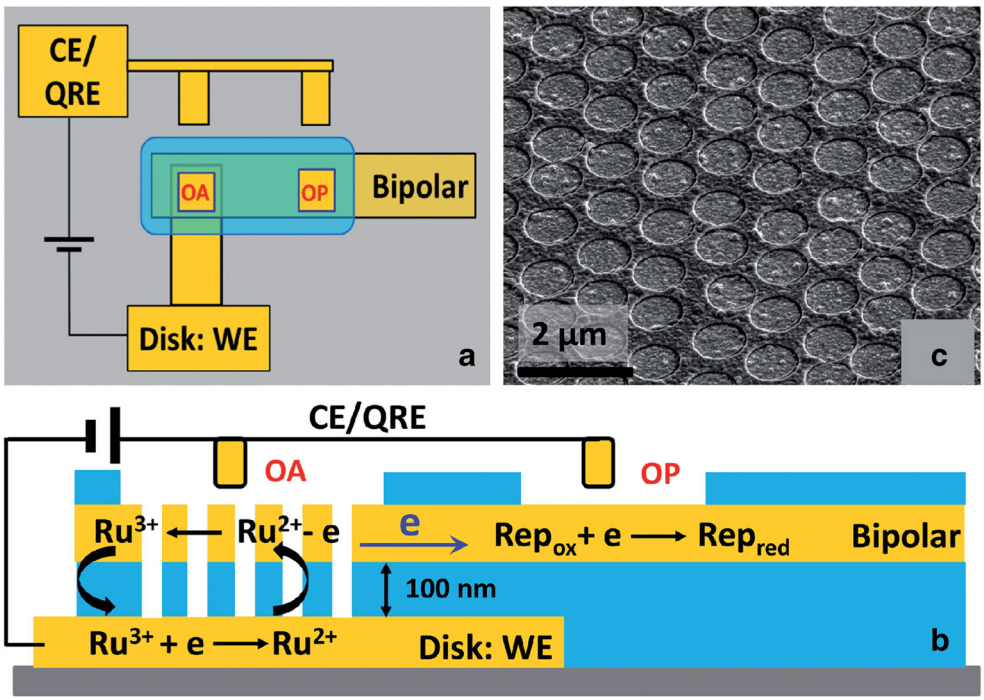

Fig. 11 **a** Schematic diagram showing a top view of the macroscopic layout of the bipolar RDE (BRDE) array and remote electrode separated by mm-distances; **b** schematic side view of the BRDE array and illustration of the mechanism of self-induced redox cycling for $Ru(NH_3)_6^{2/3+}$ (abbreviated as $Ru^{2/3+}$). SIRC in the BRDE at OA is monitored by a reporter redox couple ($Rep_{ox/red}$) at a remote location (OP); **c** SEM image of the array at 45° tilt. Reproduced from from *Chem. Sci.* 2015, 6, 3173. with permission of The Royal Society of Chemistry

pore. Simultaneously, if the ZMW is fabricated from a metal with a large ideally polarizable region, it can be used as a working electrode. Under the proper conditions, single molecule spectroelectrochemistry can be performed by coupling the electron transfer events from fluorigenic reactions to the optical behavior of the ZMW.

In an initial demonstration of the electrochemical possibilities of ZMWs, single molecules of flavin adenine dinucleotide (FAD) were functionalized in individual Au ZMW nanopores and investigated as a function of potential with wide field epi-illumination microscopy. [107] By controlling the potential, single immobilized FAD molecules were modulated between emitting (oxidized) and non-emitting (reduced) states. Examining the statistical distribution of emitting/non-emitting states over many single molecules gives insight into the single molecule dispersion in electrochemical behavior, e.g. E_{eq} variation among individual molecules. This work was extended in similar ZMWs but with freely diffusing FAD and flavin mononucleotide (FMN) by moving to confocal fluorescence geometry. Because single molecule fluorescence bursts could be measured down to the μs-timescale, the problem posed by μs residence times of freely diffusing molecules in single ZMW nanopores was circumvented, and single molecule fluorescence analogs of scanned potential experiments, in particular chronofluorometry and cyclic potential sweep fluorescence, were realized, showing the power single molecule spectroscopy applied to electrochemical experiments. [73].

Nanoscale ion transfer at immiscible interfaces The electrochemical behavior of immiscible liquid-liquid interfaces, especially the ability to study ion transfer across the interface, has been of interest for some time. Arrigan and coworkers have pioneered the translation of this experiment to nanoscale interfaces between two immiscible electrolyte solutions, i.e. nanoITIES arrays. [108–111] Produced primarily with FIB milling, ion transfer can be electrochemically monitored across the nanoarray. Figure 12 illustrates the tight relationship between nanopore geometry and electrochemical performance by showing the ion transfer current density for various arrays and the relationship between sensitivity and pore size. The sensitivity of ion transfer across the phase boundary increases as the size of the nanopores decreases, providing ample motivation for moving to nanoscale interfaces. [112, 113] Similar to other nanoelectrode array devices, maintaining diffusional independence between electrodes is an important consideration in order to maximize signal. [114] The expected limiting current for nanoITIES arrays is given by,

$$I = 4zFDcrN \quad (7)$$

where z is the charge, D is the diffusion coefficient, c is the bulk concentration, r is the radius of the nanopore, and N is total number of pores in the array. [114–116] Recently, independent radial diffusion for nanoITIES array devices was shown to occur when the interpore distance to pore diameter ratio is greater than ~50. These devices show promise as new types of electrochemical sensors.

Future outlook

Nanopore- and nanochannel-based electrode arrays are particularly promising for electrochemical applications with

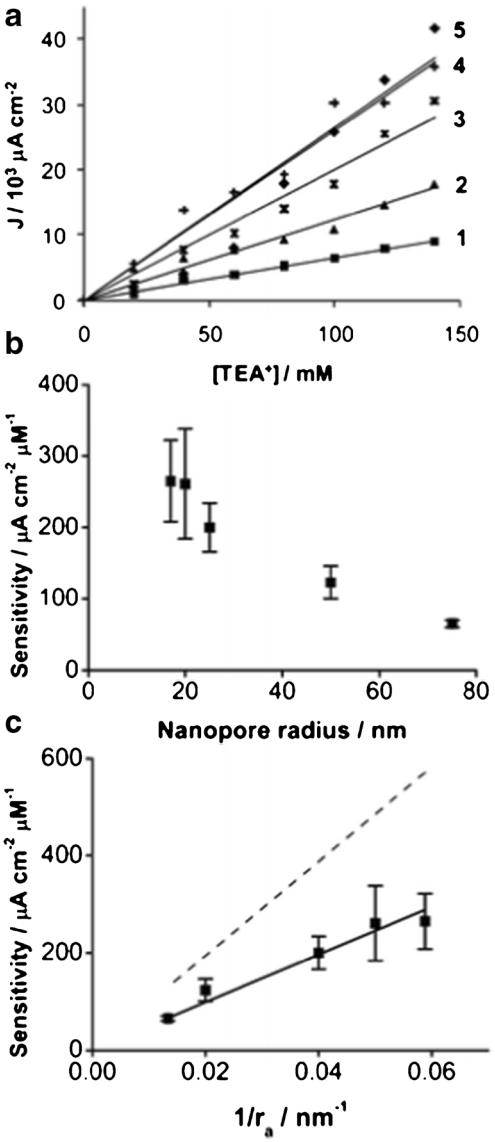

Fig. 12 **a** Forward scan ion transfer current density (J, μA cm^{-2}) vs. TEA^+ concentration (μM) for each nanointerface array, based on nanopore design: 1 (■), 2(▲), 3(×), 4(♦) and 5 (+). **b** Sensitivity of the nanointerface array (μA cm^{-2} μM^{-1}) as a function of the nanopore radius r_a (nm) used to form the nanointerface. **c** Sensitivity (μA cm^{-2} μM^{-1}) as a function of r_a^{-1}, compared to theory (dashed line). The error bars in (**b**) and **c** were calculated from the standard deviations of the slopes of the calibration curves in (**a**). Reproduced from *Analyst* 2011, 136, 4674. with permission of The Royal Society of Chemistry

enhanced performance, e.g. lower limits of detection and improved selectivity, by taking advantage of novel modes of operation, such as coupled single molecule spectroscopy and redox cycling that are uniquely enabled in nanoscale structures. The ultimate level of sensitivity, allowing the electrochemical behavior of single redox-active molecules to be studied, is attainable in these types of nanopore-based devices. Thus, the enhanced analytical performance metrics of these nanoelectrode arrays presage great advances for the future. The greatest remaining challenge in the development of nanoelectrode arrays is fabrication. In particular, the translation of small batch fabrication to large-scale, cost-effective production remains a barrier to widespread adaption of nanopore- and nanochannel-based electrode arrays for sensing and testing applications, but this too should yield to ever more clever and intricate experimental approaches.

Acknowledgments Work described herein that was carried out in the authors' laboratories was supported by the National Science Foundation, most recently through grant 1404744 and by the Department of Energy Basic Energy Sciences through grant DE FG02 07ER15851. Fabrication and structural characterization of the devices studied here were accomplished at the Notre Dame Nanofabrication Facility and the Notre Dame Integrated Imaging Facility whose generous support is gratefully acknowledged.

References

1. Liu CY, Gillette EI, Chen XY, Pearse AJ, Kozen AC, Schroeder MA, Gregorczyk KE, Lee SB, Rubloff GW (2014) An all-in-one nanopore battery array. Nat Nanotechnol 9(12):1031–1039
2. Hees J, Hoffmann R, Kriele A, Smirnov W, Obloh H, Glorer K, Raynor B, Driad R, Yang NJ, Williams OA, Nebel CE (2011) Nanocrystalline diamond nanoelectrode arrays and ensembles. ACS Nano 5(4):3339–3346
3. Dawson K, O'Riordan A (2014) Electroanalysis at the nanoscale. Annu Rev Anal Chem 7:163–181
4. Wahl A, Barry S, Dawson K, MacHale J, Quinn AJ, O'Riordan A (2014) Electroanalysis at ultramicro and nanoscale electrodes: a comparative study. J Electrochem Soc 161(2):B3055–B3060
5. Oja SM, Wood M, Zhang B (2013) Nanoscale electrochemistry. Anal Chem 85(2):473–486
6. Murray RW (2008) Nanoelectrochemistry: metal nanoparticles, nanoelectrodes, and nanopores. Chem Rev 108(7):2688–2720
7. Arrigan DWM (2004) Nanoelectrodes, nanoelectrode arrays and their applications. Analyst 129(12):1157–1165
8. LaFratta CN, Walt DR (2008) Very high density sensing arrays. Chem Rev 108(2):614–637
9. Li T, Hu WP (2011) Electrochemistry in nanoscopic volumes. Nanoscale 3(1):166–176
10. Bae JH, Han JH, Chung TD (2012) Electrochemistry at nanoporous interfaces: new opportunity for electrocatalysis. Phys Chem Chem Phys 14(2):448–463
11. Xiao X, Roberts ME, Wheeler DR, Washburn CM, Edwards TL, Brozik SM, Montano GA, Bunker BC, Burckel DB, Polsky K (2010) Increased mass transport at lithographically defined 3-D porous carbon electrodes. ACS Appl Mater Inter 11:3179–3184
12. Ueno K, Hayashida M, Ye JY, Misawa H (2005) Fabrication and electrochemical characterization of interdigitated nanoelectrode arrays. Electrochem Commun 7(2):161–165
13. Schmueser I, Walton AJ, Terry JG, Woodvine HL, Freeman NJ, Mount AR (2013) A systematic study of the influence of nanoelectrode dimensions on electrode performance and the implications for electroanalysis and sensing. Faraday Discuss 164: 295–314
14. Rauf S, Shiddiky MJA, Asthana A, Dimitrov K (2012) Fabrication and characterization of gold nanohole electrode arrays. Sensors Actuators B Chem 173:491–496
15. Moretto LM, Tormen M, Carpentiero A, Ugo P (2010) Arrays of nanoelectrodes. Critical evaluation of geometrical and diffusion characteristics with respect to electroanalytical applications. ECS Trans 25(28):33–38
16. Molina A, Laborda E, Gonzalez J, Compton RG (2013) Effects of convergent diffusion and charge transfer kinetics on the diffusion layer thickness of spherical micro- and nanoelectrodes. Phys Chem Chem Phys 15(19):7106–7113
17. Godino N, Borrise X, Munoz FX, del Campo FJ, Compton RG (2009) Mass transport to nanoelectrode arrays and limitations of the diffusion domain approach: theory and experiment. J Phys Chem C 113(25):11119–11125
18. Henstridge MC, Compton RG (2012) Mass transport to micro- and nanoelectrodes and their arrays: a review. Chem Rec 12(1): 63–71
19. Freeman NJ, Sultana R, Reza N, Woodvine H, Terry JG, Walton AJ, Brady CL, Schmueser I, Mount AR (2013) Comparison of the performance of an array of nanoband electrodes with a macro electrode with similar overall area. Phys Chem Chem Phys 15(21):8112–8118
20. Lanyon YH, De Marzi G, Watson YE, Quinn AJ, Gleeson JP, Redmond G, Arrigan DWM (2007) Fabrication of nanopore array electrodes by focused ion beam milling. Anal Chem 79(8):3048–3055
21. Lanyon YH, Arrigan DWM (2007) Recessed nanoband electrodes fabricated by focused ion beam milling. Sensors Actuators B Chem 121(1):341–347
22. Triroj N, Jaroenapibal P, Beresford R (2013) Gas-assisted focused ion beam fabrication of gold nanoelectrode arrays in electron-beam evaporated alumina films for microfluidic electrochemical sensors. Sensors Actuators B Chem 187:455–460
23. Lillo M, Losic D (2009) Ion-beam pore opening of porous anodic alumina: the formation of single nanopore and nanopore arrays. Mater Lett 63(3–4):457–460
24. Errachid A, Mills CA, Pla-Roca M, Lopez MJ, Villanueva G, Bausells J, Crespo E, Teixidor F, Samitier J (2008) Focused ion beam production of nanoelectrode arrays. Mat Sci Eng C-Bio S 28(5–6):777–780
25. Sandison ME, Cooper JM (2006) Nanofabrication of electrode arrays by electron-beam and nanoimprint lithographies. Lab Chip 6(8):1020–1025
26. Ma CX, Contento NM, Gibson LR, Bohn PW (2013) Redox cycling in nanoscale-recessed ring-disk electrode arrays for enhanced electrochemical sensitivity. ACS Nano 7(6):5483–5490
27. Wong TI, Han S, Wu L, Wang Y, Deng J, Tan CYL, Bai P, Loke YC, Yang XD, Tse MS, Ng SH, Zhou XD (2013) High throughput and high yield nanofabrication of precisely designed gold nanohole arrays for fluorescence enhanced detection of biomarkers. Lab Chip 13(12):2405–2413
28. Menon VP, Martin CR (1995) Fabrication and evaluation of nanoelectrode ensembles. Anal Chem 67(13):1920–1928
29. Hulteen JC, Martin CR (1997) A general template-based method for the preparation of nanomaterials. J Mater Chem 7(7):1075–1087

30. Brumlik CJ, Martin CR, Tokuda K (1992) Microhole array electrodes based on microporous alumina membranes. Anal Chem 64(10):1201–1203
31. Penner RM, Martin CR (1987) Preparation and electrochemical characterization of ultramicroelectrode ensembles. Anal Chem 59(21):2625–2630
32. Valsesia A, Lisboa P, Colpo P, Rossi F (2006) Fabrication of polypyrrole-based nanoelectrode arrays by colloidal lithography. Anal Chem 78(21):7588–7591
33. Bai JW, Wang DQ, Nam SW, Peng HB, Bruce R, Gignac L, Brink M, Kratschmer E, Rossnagel S, Waggonerl P, Reuter K, Wang C, Astier Y, Balagurusamy V, Luan BQ, Kwark Y, Joseph E, Guillorn M, Polonsky S, Royyuru A, Rao SP, Stolovitzky G (2014) Fabrication of sub-20 nm nanopore arrays in membranes with embedded metal electrodes at wafer scales. Nanoscale 6(15): 8900–8906
34. Gholizadeh A, Shahrokhian S, Zad AI, Mohajerzadeh S, Vosoughi M, Darbari S, Koohsorkhi J, Mehran M (2012) Fabrication of sensitive glutamate biosensor based on vertically aligned CNT nanoelectrode array and investigating the effect of CNTs density on the electrode performance. Anal Chem 84(14):5932–5938
35. Zhang XJ, Wang J, Ogorevc B, Spichiger UE (1999) Glucose nanosensor based on prussian-blue modified carbon-fiber cone nanoelectrode and an integrated reference electrode. Electroanal 11(13):945–949
36. Yu JC, Zhang YJ, Liu SQ (2014) Enzymatic reactivity of glucose oxidase confined in nanochannels. Biosens Bioelectron 55:307–312
37. Dawson K, Baudequin M, O'Riordan A (2011) Single on-chip gold nanowires for electrochemical biosensing of glucose. Analyst 136(21):4507–4513
38. Claussen JC, Wickner MM, Fisher TS, Porterfield DM (2011) Transforming the fabrication and biofunctionalization of gold nanoelectrode arrays into versatile electrochemical glucose biosensors. Acs Appl Mater Inter 3(5):1765–1770
39. Lupu A, Lisboa P, Valsesia A, Colpo P, Rossi F (2009) Hydrogen peroxide detection nanosensor array for biosensor development. Sensors Actuators B Chem 137(1):56–61
40. Karyakin AA, Puganova EA, Budashov IA, Kurochkin IN, Karyakina EE, Levchenko VA, Matveyenko VN, Varfolomeyev SD (2004) Prussian blue based nanoelectrode arrays for H2O2 detection. Anal Chem 76(2):474–478
41. Sultana R, Reza N, Kay NJ, Schmueser I, Walton AJ, Terry JG, Mount AR, Freeman NJ (2014) Practical implications of using nanoelectrodes for bioanalytical measurements. Electrochim Acta 126:98–103
42. Liu JP, Guo CX, Li CM, Li YY, Chi QB, Huang XT, Liao L, Yu T (2009) Carbon-decorated ZnO nanowire array: a novel platform for direct electrochemistry of enzymes and biosensing applications. Electrochem Commun 11(1):202–205
43. Wang YL, Zhu YC, Zeng Y (2012) Amperometric biosensor based on 3D ordered freestanding porous Pt nanowire array electrode. Nanoscale 4(19):6025–6031
44. Triroj N, Jaroenapibal P, Shi HB, Yeh JI, Beresford R (2011) Microfluidic chip-based nanoelectrode array as miniaturized biochemical sensing platform for prostate-specific antigen detection. Biosens Bioelectron 26(6):2927–2933
45. Koehne JE, Marsh M, Boakye A, Douglas B, Kim IY, Chang SY, Jang DP, Bennet KE, Kimble C, Andrews R, Meyyappan M, Lee KH (2011) Carbon nanofiber electrode array for electrochemical detection of dopamine using fast scan cyclic voltammetry. Analyst 136(9):1802–1805
46. Jung HS, Kim JM, Park JW, Lee HY, Kawai T (2005) Amperometric immunosensor for direct detection based upon functional lipid vesicles immobilized on nanowell array electrode. Langmuir 21(13):6025–6029
47. Lu JS, Li HN, Cui DM, Zhang YJ, Liu SQ (2014) Enhanced enzymatic reactivity for electrochemically driven drug metabolism by confining cytochrome P450 enzyme in TiO2 nanotube arrays. Anal Chem 86(15):8003–8009
48. Swisher LZ, Syed LU, Prior AM, Madiyar FR, Carlson KR, Nguyen TA, Hua DH, Li J (2013) Electrochemical protease biosensor based on enhanced AC voltammetry using carbon nanofiber nanoelectrode arrays. J Phys Chem C 117(8):4268–4277
49. Koehne J, Li J, Cassell AM, Chen H, Ye Q, Ng HT, Han J, Meyyappan M (2004) The fabrication and electrochemical characterization of carbon nanotube nanoelectrode arrays. J Mater Chem 14(4):676–684
50. Koehne J, Li J, Chen H, Cassell A, Ng HT, Fan W, Li Q, Han J, Mayyappan M (2003) Carbon nanotube nanoelectrode array for ultrasensitive DNA detection. Nano Lett 3(5):597–602
51. Li SJ, Li J, Wang K, Wang C, Xu JJ, Chen HY, Xia XH, Huo Q (2010) A nanochannel array-based electrochemical device for quantitative label-free DNA analysis. ACS Nano 4(11):6417–6424
52. Periyakaruppan A, Gandhiraman RP, Meyyappan M, Koehne JE (2013) Label-free detection of cardiac troponin-I using carbon nanofiber based nanoelectrode arrays. Anal Chem 85(8):3858–3863
53. Zhuo L, Huang Y, Cheng MS, Lee HK, Toh CS (2010) Nanoarray membrane sensor based on a multilayer design for sensing of water pollutants. Anal Chem 82(11):4329–4332
54. Liu GD, Lin YH, Tu Y, Ren ZF (2005) Ultrasensitive voltammetric detection of trace heavy metal ions using carbon nanotube nanoelectrode array. Analyst 130(7):1098–1101
55. Branagan SP, Contento NM, Bohn PW (2012) Enhanced mass transport of electroactive species to annular nanoband electrodes embedded in nanocapillary array membranes. J Am Chem Soc 134(20):8617–8624
56. Gibson LR, Branagan SP, Bohn PW (2013) Convective delivery of electroactive species to annular nanoband electrodes embedded in nanocapillary-array membranes. Small 9(1):90–97
57. Zaino LP, Contento NM, Branagan SP, Bohn PW (2014) Coupled electrokinetic transport and electron transfer at annular nanoband electrodes embedded in cylindrical nanopores. ChemElectroChem 1(9):1570–1576
58. Contento NM, Branagan SP, Bohn PW (2011) Electrolysis in nanochannels for in situ reagent generation in confined geometries. Lab Chip 11(21):3634–3641
59. Perera DMNT, Pandey B, Ito T (2011) Electrochemical impedance spectroscopy studies of organic-solvent-induced permeability changes in nanoporous films derived from a cylinder-forming diblock copolymer. Langmuir 27(17):11111–11117
60. Li YX, Maire HC, Ito T (2007) Electrochemical characterization of nanoporous films fabricated from a polystyrene-poly(methylmethacrylate) diblock copolymer: monitoring the removal of the PMMA domains and exploring the functional groups on the nanopore surface. Langmuir 23(25):12771–12776
61. Li YX, Ito T (2009) Size-exclusion properties of nanoporous films derived from polystyrene-poly(methylmethacrylate) diblock copolymers assessed using direct electrochemistry of ferritin. Anal Chem 81(2):851–855
62. Li CY, Tian YW, Shao WT, Yuan CG, Wang K, Xia XH (2014) Solution pH regulating mass transport in highly ordered nanopore array electrode. Electrochem Commun 42:1–5
63. Kim S, Polycarpou AA, Liang H (2014) Enhanced-ion transfer via metallic-nanopore electrodes. J Electrochem Soc 161(10):A1475–A1479
64. Ito T, Audi AA, Dible GP (2006) Electrochemical characterization of recessed nanodisk-array electrodes prepared from track-etched membranes. Anal Chem 78(19):7048–7053

65. Perera DMNT, Ito T (2010) Cyclic voltammetry on recessed nanodisk-array electrodes prepared from track-etched polycarbonate membranes with 10-nm diameter pores. Analyst 135(1):172–176
66. Jeoung E, Galow TH, Schotter J, Bal M, Ursache A, Tuominen MT, Stafford CM, Russell TP, Rotello VM (2001) Fabrication and characterization of nanoelectrode arrays formed via block copolymer self-assembly. Langmuir 17(21):6396–6398
67. Tokuda K, Morita K, Shimizu Y (1989) Cyclic voltammetry at microhole array electrodes. Anal Chem 61(15):1763–1768
68. Bond AM, Luscombe D, Oldham KB, Zoski CG (1988) A comparison of the chronoamperometric response at inlaid and recessed disk microelectrodes. J Electroanal Chem Interfacial Electrochem 249(1–2):1–14
69. Yu JC, Luo PC, Xin CX, Cao XD, Zhang YJ, Liu SQ (2014) Quantitative evaluation of biological reaction kinetics in confined nanospaces. Anal Chem 86(16):8129–8135
70. Shibata Y, Morita M (1989) Exchange of comments on identification and quantitation of arsenic species in a dogfish muscle reference material for trace-elements. Anal Chem 61(18):2116–2118
71. Chow K-F, Mavre F, Crooks JA, Chang B-Y, Crooks RM (2009) A large-scale, wireless electrochemical bipolar electrode microarray. J Am Chem Soc 131(24):8364–8365
72. Mavre F, Anand RK, Laws DR, Chow K-F, Chang B-Y, Crooks JA, Crooks RM (2010) Snapshot voltammetry using a triangular bipolar microelectrode. Anal Chem 82(12):8766–8774
73. Zaino LP, Grismer DA, Han D, Crouch GM, Bohn PW (2015) Single occupancy spectroelectrochemistry of freely diffusing flavin mononucleotide in zero-dimensional nanophotonic structures. Faraday Discuss. doi:10.1039/C5FD00072F
74. Niwa O, Tabei H (1994) Voltammetric measurements of reversible and quasi-reversible redox species using carbon film based interdigitated array microelectrodes. Anal Chem 66(2):285–289
75. Hayashi K, Takahashi J, Horiuchi T, Iwasaki Y, Haga T (2008) Development of nanoscale interdigitated array electrode as electrochemical sensor platform for highly sensitive detection of biomolecules. J Electrochem Soc 155(9):J240–J243
76. Goluch ED, Wolfrum B, Singh PS, Zevenbergen MAG, Lemay SG (2009) Redox cycling in nanofluidic channels using interdigitated electrodes. Anal Bioanal Chem 394(2):447–456
77. Rahimi M, Mikkelsen SR (2011) Cyclic biamperometry at microinterdigitated electrodes. Anal Chem 83(19):7555–7559
78. Fan F-RF, Bard AJ (1995) Electrochemical detection of single molecules. Science 267(5199):871–871
79. Paixao TRLC, Richter EM, Brito-Neto JGA, Bertotti M (2006) Fabrication of a new generator-collector electrochemical microdevice: characterization and applications. Electrochem Commun 8:9–14
80. Wolfrum B, Zevenbergen M, Lemay S (2008) Nanofluidic redox cycling amplification for the selective detection of catechol. Anal Chem 80:972–977
81. Straver MG, Odijk M, Olthuis W, van den Berg A (2012) A simple method to fabricate electrochemical sensor systems with predictable high-redox cycling amplification. Lab Chip 12:1548–1553
82. Aguilar ZP, Vandaveer WR, Fritsch I (2002) Self-contained microelectrochemical immunoassay for small volumes using mouse IgG as a model system. Anal Chem 74:3321–3329
83. Vandaveer WR, Woodward DJ, Fritsch I (2003) Redox cycling measurements of a model compound and dopamine in ultrasmall volumes with a self-contained microcavity device. Electrochim Acta 48:3341–3348
84. Neugebauer S, Mueller U, Lohmueller T, Spatz JP, Stelzle M, Schuhmann W (2006) Characterization of nanopore electrode structures as basis for amplified electrochemical assays. Electroanal 18:1929–1936
85. Menshykau D, del Campo FJ, Munoz FX, Compton RG (2009) Current collection efficiency of micro- and nano-ring-recessed disk electrodes and of arrays of these electrodes. Sensors Actuators B B138:362–367
86. Menshykau D, O'Mahony AM, del Campo FJ, Munoz FX, Compton RG (2009) Microarrays of ring-recessed disk electrodes in transient generator-collector mode: theory and experiment. Anal Chem 81:9372–9382
87. Ma C, Contento NM, Gibson LR, Bohn PW (2013) Recessed ring-disk nanoelectrode arrays integrated in nanofluidic structures for selective electrochemical detection. Anal Chem 85(20):9882–9888
88. Ma CX, Contento NM, Bohn PW (2014) Redox cycling on recessed ring-disk nanoelectrode arrays in the absence of supporting electrolyte. J Am Chem Soc 136(20):7225–7228
89. Zhu F, Yan J-W, Lu M, Zhou Y-L, Yang Y, Mao B-W (2011) A strategy for selective detection based on interferent depleting and redox cycling using the plane-recessed microdisk array electrodes. Electrochim Acta 56:8101–8107
90. Hüske M, Stockmann R, Offenhäusser A, Wolfrum B (2014) Redox cycling in nanoporous electrochemical devices. Nanoscale 6(1):589–598
91. Zevenbergen MAG, Wolfrum BL, Goluch ED, Singh PS, Lemay SG (2009) Fast electron-transfer kinetics probed in nanofluidic channels. J Am Chem Soc 131:11471–11477
92. Sun P, Mirkin MV (2008) Electrochemistry of individual molecules in zeptoliter volumes. J Am Chem Soc 130(26):8241–8250
93. Henry CS, Fritsch I (1999) Microcavities containing individually addressable recessed microdisk and tubular nanoband electrodes. J Electrochem Soc 146(9):3367–3373
94. Ma CX, Zaino LP, Bohn PW (2015) Self-induced redox cycling coupled luminescence on nanopore recessed disk-multiscale bipolar electrodes. Chem Sci 6(5):3173–3179
95. Zhu F, Yan J, Pang S, Zhou Y, Mao B, Oleinick A, Svir I, Amatore C (2014) Strategy for increasing the electrode density of microelectrode arrays by utilizing bipolar behavior of a metallic film. Anal Chem 86(6):3138–3145
96. Dam VAT, Olthuis W, van den Berg A (2007) Redox cycling with facing interdigitated array electrodes as a method for selective detection of redox species. Analyst 132:365–370
97. Schoch RB, Renaud P (2005) Ion transport through nanoslits dominated by the effective surface charge. Appl Phys Lett 86(25):253111
98. Watkins JJ, White HS (2004) The role of the electrical double layer and ion pairing on the electrochemical oxidation of hexachloroiridate(III) at Pt electrodes of nanometer dimensions. Langmuir 20:5474–5483
99. Stein D, Kruithof M, Dekker C (2004) Surface-charge-governed ion transport in nanofluidic channels. Phys Rev Lett 93(3):035901
100. Myers D (1999) Surfaces, interfaces, and colloids. Wiley-Vch New York
101. Horiuchi T, Niwa O, Morita M, Tabei H (1991) Limiting current enhancement by self-induced redox cycling on a micro-macro twin electrode. J Electrochem Soc 138:3549–3553
102. Horiuchi T, Niwa O, Morita M, Tabei H (1992) Stripping voltammetry of reversible redox species by self-induced redox cycling. Anal Chem 64:3206–3208
103. Tabei H, Horiuchi T, Niwa O, Morita M (1992) Highly sensitive detection of reversible species by self-induced redox cycling. J Electroanal Chem 326:339–343
104. Horiuchi T, Niwa O, Tabei H (1994) Detection of reversible redox species by substitutional stripping voltammetry. Anal Chem 66: 1224–1230

105. Morita M, Niwa O, Horiuchi T (1997) Interdigitated array microelectrodes as electrochemical sensors. Electrochim Acta 42:3177–3183
106. Oleinick A, Zhu F, Yan J, Mao B, Svir I, Amatore C (2013) Theoretical investigation of generator-collector microwell arrays for improving electroanalytical selectivity: application to selective dopamine detection in the presence of ascorbic acid. ChemPhysChem 14:1887–1898
107. Zhao J, Zaino LP, Bohn PW (2013) Potential-dependent single molecule blinking dynamics for flavin adenine dinucleotide covalently immobilized in zero-mode waveguide array of working electrodes. Faraday Discuss 164:57–69
108. Scanlon MD, Strutwolf J, Blake A, Iacopino D, Quinn AJ, Arrigan DWM (2010) Ion-transfer electrochemistry at arrays of nanointerfaces between immiscible electrolyte solutions confined within silicon nitride nanopore membranes. Anal Chem 82(14): 6115–6123
109. Sairi M, Strutwolf J, Mitchell RA, Silvester DS, Arrigan DWM (2013) Chronoamperometric response at nanoscale liquid-liquid interface arrays. Electrochim Acta 101:177–185
110. Sairi M, Chen-Tan N, Neusser G, Kranz C, Arrigan DWM (2015) Electrochemical characterisation of nanoscale liquid jLiquid interfaces located at focused ion BeamMilled silicon nitride membranes. ChemElectroChem 2(1):98–105
111. Liu Y, Strutwolf J, Arrigan DWM (2015) Ion-transfer voltammetric behavior of propranolol at nanoscale liquid-liquid interface arrays. Anal Chem 87(8):4487–4494
112. Rimboud M, Hart RD, Becker T, Arrigan DWM (2011) Electrochemical behaviour and voltammetric sensitivity at arrays of nanoscale interfaces between immiscible liquids. Analyst 136(22):4674–4681
113. Scanlon MD, Arrigan DWM (2011) Enhanced electroanalytical sensitivity via interface miniaturisation: ion transfer voltammetry at an array of nanometre liquid-Liquid Interfaces. Electroanal 23(4):1023–1028
114. Liu Y, Sairi M, Neusser G, Kranz C, Arrigan DWM (2015) Achievement of diffusional independence at nanoscale liquid liquid interfaces within arrays. Anal Chem 87(11):5486–5490
115. Saito Y (1968) A theoretical study on the diffusion current at the stationary electrodes of circular and narrow band types. Rev Polarogr 15(6):177–187
116. Soos ZG, Lingane PJ (1964) Derivation of chronoamperometric constant for unshielded circular planar electrodes. J Phys Chem 68(12):3821–3828